Available online at www.sciencedirect.com
ScienceDirect
International Journal of Thermal Sciences 48 (2009) 733–746
International Journal of Thermal Sciences
www.elsevier.com/locate/ijts

Numerical study of flow and energy fields in thermoacoustic couples of non-zero thickness

L. Zoontjens *, C.Q. Howard, A.C. Zander, B.S. Cazzolato

School of Mechanical Engineering, The University of Adelaide, South Australia

Received 31 July 2007; received in revised form 15 June 2008; accepted 16 June 2008

Available online 10 July 2008

Abstract

A limitation in many previous numerical studies of thermoacoustic couples has been the use of stack plates which are of zero thickness. In this study, a system for modelling thermoacoustic couples of non-zero thickness is presented and implemented using a commercial CFD code. The effect of increased drive-ratio and plate thickness upon the time-average heat transfer through the stack material is investigated. Results indicate that the plate thickness strongly controls the generation of vortices outside the stack region, perturbing the flow structure and heat flux distribution at the extremities of the plate. An increase in plate thickness is also shown to improve the spatial integral of the total heat transfer rate but at the expense of increased entropy generation.

Keywords: Thermoacoustics; Heat; Sound; Thermoacoustic couples; Heat exchangers; Acoustic streaming

1. Introduction

In a time of increased concern over environmental impact and operating costs of refrigeration systems, thermoacoustic refrigeration technologies are appearing more and more attractive for commercialisation. These devices possess efficiencies comparable to conventional vapour-compression systems, and operate without adverse environmental impact, significant maintenance requirements or high construction costs. Thermoacoustic refrigeration units can be driven using heat as a direct input energy source, and as such are appealing for waste energy recovery from heat sources such as hot exhaust gas streams from existing thermodynamic processes or solar collectors.

Swift [1,2] has published detailed information regarding the design and operation of practical thermoacoustic systems and modern summaries of the classical works of Rott [3] and colleagues. These publications primarily concern what is referred to commonly as the 'linear theory' in which the thermoacoustic device is represented using one-dimensional acoustic formulations. When optimising new thermoacoustic devices, most designs make use of linear order prediction tools such as the computer program *DeltaEC* [4] or analytical design guides [5]. There are many publications demonstrating the usefulness of these methods in the design and modelling of thermoacoustic devices [2,6–9]. However, these studies also show via experimental data that at higher operating states, the accuracy of linear prediction methods deteriorates. Higher-order numerical models may therefore assist in the understanding of various non-linear loss mechanisms during operation.

The vast proportion of two-dimensional numerical studies specific to thermoacoustic devices in the literature [10–16] have modelled what Wheatley et al. [17] termed a 'thermoacoustic couple' (TAC), which in its most abstract form is a single infinitely wide plate in an oscillatory flow field. In practice, thermoacoustic couples are best described as consisting of only a few parallel plates much shorter than the acoustic wavelength inside the resonator duct. Presumably, the thermoacoustic couple is intended to be a two-dimensional approximation of a stack consisting of a series of parallel plates. The majority of numerical studies of thermoacoustic couples assume infinite periodicity (infinite number of plates) in the transverse direction of the duct. Infinite periodicity infers that the flow structure in the vicinity of the plate may therefore be periodic and/or sym-

* Corresponding author. Tel.: +61 8 8303 5460.
E-mail address: luke.zoontjens@adelaide.edu.au (L. Zoontjens).

1290-0729/$ – see front matter
doi:10.1016/j.ijthermalsci.2008.06.007

Nomenclature

a	gas sound speed	m/s
A	cross-sectional area	m^2
BR	blockage ratio	
c_{pk}	gas heat capacity	J/kg K
c_{ps}	plate material heat capacity	J/kg K
DR	drive-ratio	
$\dot{e}_{\text{diss}}$	rate of energy dissipation	W
f	frequency, also thermal function	Hz
$\langle \dot{h}_{hx} \rangle_t$	time-average heat flux over heat exchanger boundary	W/m^2
$\langle \dot{h}_x \rangle_t$	time-average heat flux in the x-direction	W/m^2
$\langle \dot{h}_y \rangle_t$	time-average heat flux in the y-direction	W/m^2
k	gas wavenumber	m^{-1}
k_s	plate thermal conductivity	W/m K
k_0	gas thermal conductivity	W/m K
L_A	axial length of subdomain 'A'	m
L_B	axial length of subdomain 'B'	m
L_{CV}	axial length of control volume	m
L_S	stack plate length	m
M	Mach number	
M_a	acoustic Mach number	
$N_{R,S}$	streaming (oscillatory) Reynolds number	
$N^c_{R,S}$	critical streaming Reynolds number	
n_x	number of mesh grid intervals along edge in x-direction	
n_y	number of mesh grid intervals along edge in y-direction	
p_A	pressure amplitude at pressure antinode	Pa
p_m	mean operating pressure	Pa
Pr	Prandtl number	
$\lvert p_1 \rvert$	first-order acoustic pressure amplitude	Pa
$\dot{q}$	surface heat flux	W/m^2
r	internal radius	m
s	entropy	J/kg K
S	total system entropy	J/kg K
$\dot{s}_{\text{gen}}$	rate of entropy generation per unit volume	W/m^3 K
t	time	s
T_k	gas temperature	K
T_m	mean temperature	K
ts	time step	
T_s	stack temperature	K
T_0	ambient temperature	K
$\lvert u_1 \rvert$	first-order acoustic velocity amplitude	m/s
u	velocity, velocity component in x-direction	m/s
$\lvert U_1 \rvert$	first-order volumetric flow rate amplitude	m^3/s
v	velocity component in y direction	m/s
x	axial co-ordinate/dimension	m
x'	axial distance from centre of resonator	m
y	transverse co-ordinate/dimension	m
y_{hxsf}	y co-ordinate of plate surface	m
y_0	stack plate half-spacing	m
y_x	stack plate half-thickness	m

Greek letters

γ	ratio of specific heats	
$\delta_{\kappa m}$	mean thermal penetration depth	m
δ_κ	thermal penetration depth	m
δ_υ	viscous penetration depth	m
$\Delta T_{k,hx}$	axial gas temperature difference across heat exchanger	K
Δx	mesh interval spacing in x-direction	m
Δy	mesh interval spacing in y-direction	m
λ	wavelength	m
ρ	density	kg/m^3
ω	angular frequency ($=2\pi f$)	rad/s
μ	dynamic viscosity	kg/ms
ρ_s	density of the stack material	kg/m^3
υ	kinematic viscosity	m^2/s
ξ_c	normalised stack centre position	

metrical in the transverse direction. On this basis, in general only one side of infinitely wide stack plate is modelled on a boundary to a two-dimensional computational domain. Using this approach, recent numerical studies [10–16] have considered the influence of various stack geometries and flow conditions upon the performance of a parallel plate stack.

The studies by Besnoin [12] and Blanc-Benon et al. [18] are perhaps the most insightful of recent investigations of thermoacoustic stacks, since they directly compare results from both experimental and computational investigations. The dissertation of Besnoin demonstrates reasonably good agreement in flow structure between numerical results and the experimental data of Duffourd [19]. Blanc-Benon et al. compared particle image velocimetry (PIV) measurements with low Mach number flow computational results for a small region at one end of a thermoacoustic stack. The study also showed that the computational model gave reasonably good predictions of the flow structure as determined experimentally. A later study by El-Gendy et al. [20] of a miniature thermoacoustic refrigerator design also used PIV data in their optimisation considerations, which suggests there is increasing research interest in the flow structures present within thermoacoustic devices.

The cross-sectional geometry of a parallel plate stack may be characterised in terms of the plate thickness and plate pitch. The blockage ratio BR is defined as the ratio of open gas area to total device cross sectional area: the BR of a parallel plate stack (or thermoacoustic couple) is commonly evaluated as simply

$$BR = 1 - \frac{y_x}{y_0} \tag{1}$$

where y_0 is the half-distance between the centrelines of two adjacent plates and y_x is the plate half-thickness. The drive-ratio DR is defined as the ratio of the maximum oscillatory pressure amplitude divided by the ambient pressure p_m.

This study aims to build upon existing knowledge by implementing a commercial numerical code to investigate the effect of increased drive-ratio and plate thickness upon specific performance criteria. In addition, we seek to identify loss or gain mechanisms in thermoacoustic couples via graphical representation of flow and energy fields. The criteria used in this paper to define the performance of the thermoacoustic couple are based upon the time-averaged gas temperature difference and rate of heat transfer between the plate and working fluid.

The model presented in this study assumes symmetrical flow conditions but models finite heat conductivity and heat capacity for plates of zero and non-zero thickness. Therefore, this study is not designed to provide data that is directly comparable with existing experimental results, but rather provide insight into the effects that do influence actual outcomes.

In Section 2, the numerical model, operating conditions and performance measures considered are introduced. Results in Section 3 are presented using two different viewpoints. Section 3.1 contains discussion of the flow structures that develop, and Section 3.2 reports the influence of plate thickness upon the distribution of heat flux across the plate surface.

2. Numerical model

This study aims to build upon previous work by considering the performance of a thermoacoustic couple for varying blockage ratio *BR* and drive-ratio *DR*.

For the sake of comparison with previous studies [10,13, 16], the numerical model uses similar operating conditions but an expanded solution domain to account for physical flow disturbances. The model approximates a closed-ended, half-wavelength standing wave resonator duct filled with helium at 10 kPa absolute pressure, with a parallel-plate stack located in one end of the device. As the resonator length is fixed at 5.04 m and the sound speed of the gas at ambient temperature $T_0 = 300$ K is 1008 m/s, the operating frequency of the device is fixed to have the first natural frequency at 100 Hz.

Fig. 1 presents the computational domain in the context of the theoretical half-wavelength resonator. The resonator is shown as a two-dimensional representation of a smooth duct with rigid terminations at each end. Ignoring effects of the resonator diameter and duct surfaces, a parallel plate stack located inside the resonator is then for the purposes of this study, of infinite width and plate count. The heat transfer coefficients between the fluid and solid are calculated using a discrete Fourier law approach [23, Section 7.13.4].

2.1. Modelspace

Fig. 2 shows a sketch of the modelspace used in this study. The plate and thermal reservoir comprises subdomains 'P' and 'H', respectively. Subdomain 'S' is the region encompassed by the plate axially within the stack. The length y_0 is the half-spacing between plate centrelines. Subdomains 'A' and 'B' enable consideration of flow structures which may develop outside the stack region due to non-zero plate half-thickness y_x,

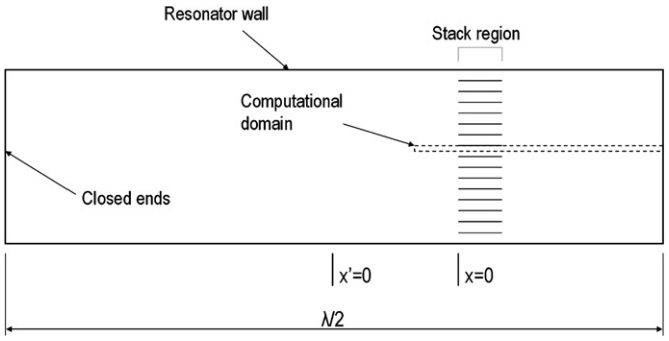

Fig. 1. Locus of the computational domain within the theoretical model of half-wavelength resonator tube with parallel plate stack. Acoustic source not shown.

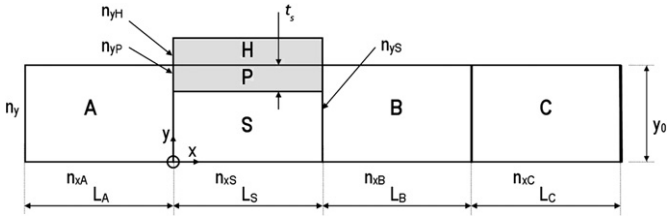

Fig. 2. Annotated sketch of the basic thermoacoustic couple modelspace. Shaded areas are regions of solid material: unshaded areas are fluid regions. The half-thickness of the plate is modelled using finite y_x, and appropriate selection of the number of mesh intervals in the x- and y-directions, n_{xP} $(= n_{xS})$ and n_{yP}.

and are of sufficient lengths L_A and L_B such that the pressure changes can be considered adiabatic. Subdomain 'C' links subdomain 'B' to the hard walled end of the duct at the right edge of subdomain 'C'. Symmetric boundary conditions have been imposed on all lateral fluid boundaries and an oscillatory boundary condition on the left side of subdomain 'A', has been used to induce an acoustic standing wave.

The inclusion of subdomain 'H' is to allow plates of zero thickness to be modelled with finite heat capacity and thermal conductivity. To provide comparative results with Ishikawa and Mee [13] and Piccolo and Pistone [16], subdomain 'P' is removed, and subdomain 'S' is of the same width (y_0) as subdomains A, B and C. In following Piccolo and Pistone [16], the top and sides of subdomain 'H' are thermally insulated, forcing any excess heat entering regions 'H' and 'P' to return back through the boundaries between subdomain 'P' and subdomains 'A', 'S' and 'B'. The thermal properties of the stack are important because unsteady temperature distributions are allowed to form within the stack region.

The thickness and hence influence of subdomain 'H' is intended to be minimal compared to that of subdomain 'P'. In terms of flow effects, the heat reservoir H does not break the transverse symmetry of the structure faced by the working fluid since it is not in contact with fluid boundaries. In terms of heat transfer, the subdomain 'H' adds a level of thermal capacitance that we consider minimal.

The number of mesh intervals in the x and y directions, n_x and n_y, respectively, can be easily adjusted to explore the grid dependency of the model or match the sizings used by previous studies. For example, in Section 2.3 where comparisons are

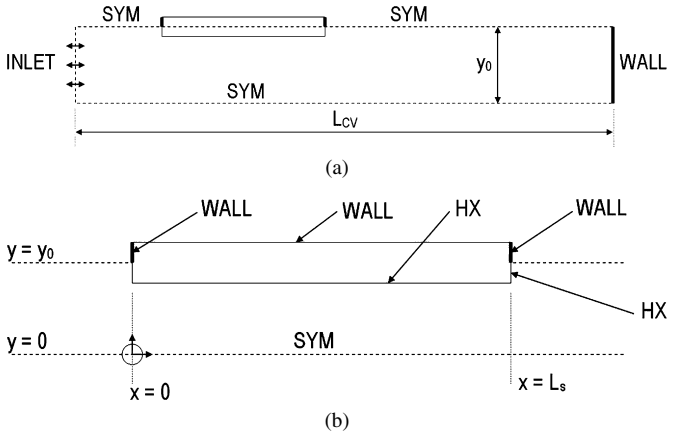

Fig. 3. Computational domains used in this study showing boundary conditions and selected geometry. (b) provides a closer view of the stack region shown in (a).

drawn with the results of Piccolo and Pistone [16], $n_{xS} = 244$ and $n_y = n_{yS} = 50$, with $L_S = 0.252$ m.

The effect of non-zero plate thickness can be accommodated by varying y_x, indicated as the vertical size of subdomain 'P'. To preserve a consistent and rectangular computational mesh, n_{yX} is increased at the expense of n_{yS} such that $n_y = n_{yX} + n_{yS}$. The transverse dimension (thickness) of subdomain 'H' was held fixed at $\Delta y = 0.16$ mm.

2.2. Boundary conditions

Fig. 3 (a) and (b) indicates the boundary types and various length scales used in this study. The conditions imposed upon the boundaries shown in Fig. 3 (a) and (b) are defined as

$$\left.\begin{array}{l} u = 0 \\ v = 0 \\ \frac{dT}{dy} = 0 \end{array}\right\} \text{ on axial 'WALL' boundaries} \tag{2}$$

$$\left.\begin{array}{l} u = 0 \\ v = 0 \\ \frac{dT}{dx} = 0 \end{array}\right\} \text{ on transverse 'WALL' boundaries} \tag{3}$$

$$\left.\begin{array}{l} u = 0 \\ v = 0 \end{array}\right\} \text{ on 'HX' boundaries} \tag{4}$$

$$\left.\begin{array}{l} v = 0 \\ \frac{dT}{dy} = 0 \end{array}\right\} \text{ on 'SYM' boundaries, and} \tag{5}$$

$$\left.\begin{array}{l} p = p_m + \mathrm{Re}\left[|p_1| e^{j(\omega t + kx' - \frac{\pi}{2})}\right] \\ \text{on 'INLET' boundaries} \end{array}\right\} \tag{6}$$

with u and v the components of velocity in the x and y directions, and x' the axial distance from the centre of the duct. Temperatures were not controlled on HX boundaries.

The axial length of subdomains 'A' and 'B' were set equal to $L_A = L_B = 0.15$ m. The axial length of the computational domain, L_{CV}, was set to 1.476 m. As shown in Fig. 1, the origin of the computational domain is located 1.194 m axially from the centre of the duct, i.e. $x' = x + 1.194$ m.

Table 1
Flow and geometry parameters for each simulation run used in investigating blockage ratio. Run 22 differs only from Run 1 in using a mesh with grid mesh sizing equivalent to that used by Piccolo and Pistone [16]. $DR = |p_1|/p_m$

Run	$\lvert p_1\rvert$ (Pa)	$\lvert p_1\rvert/p_m$ (%)	y_x (mm)	$\lambda_{\kappa m}/y_x$	*BR*
1	170	1.7	0	∞	1
2	340	3.4	0	∞	1
3	510	5.1	0	∞	1
4	680	6.8	0	∞	1
5	170	1.7	0.16	15	0.98
6	340	3.4	0.16	15	0.98
7	510	5.1	0.16	15	0.98
8	680	6.8	0.16	15	0.98
9	170	1.7	0.80	3.0	0.9
10	340	3.4	0.80	3.0	0.9
11	510	5.1	0.80	3.0	0.9
12	680	6.8	0.80	3.0	0.9
13	170	1.7	1.6	1.5	0.8
14	340	3.4	1.6	1.5	0.8
15	510	5.1	1.6	1.5	0.8
16	680	6.8	1.6	1.5	0.8
17	170	1.7	2.4	1.0	0.7
18	340	3.4	2.4	1.0	0.7
19	510	5.1	2.4	1.0	0.7
20	680	6.8	2.4	1.0	0.7
21	850	8.5	2.4	1.0	0.7
22	170	1.7	0	∞	1

2.3. Operating conditions

Throughout the computational domain, the pressure, velocity and temperature were initialised at ambient conditions, that is

$$\left.\begin{array}{l} u = 0 \\ v = 0 \\ T_k = T_m \end{array}\right\} \text{ for } t = 0 \text{ at all } x \text{ and } y \tag{7}$$

By following Ishikawa and Mee [13], where the operating frequency $f = 100$ Hz, $T_m = 300$ K and $p_m = 10$ kPa (approximately 0.1 atmospheres) for all runs, the mean thermal penetration distance $\delta_{\kappa m}$ $(= \sqrt{2k/\omega\rho c_p})$ is ≈2.4 mm for helium as the working fluid.

Flow and geometry parameters for each run are listed in Table 1. Twenty-one runs were completed covering typically four different drive-ratios for five different plate half-thicknesses y_x. In addition, Run 22 was developed to compare the current results to those published by Piccolo and Pistone [16] and hence uses the same operating conditions as Run 1, however it differs in grid mesh density.

2.4. Turbulence criteria

An approximation of the free stream 'acoustic' Mach number M_a as defined by Eq. (8) is a useful measure of the "nonlinear behaviour" of the system or an indicator of higher order acoustic modes. Eq. (9) is a modification of Eq. (8) to compensate somewhat for the effect of blockage ratio *BR* within stack

pores: this follows from the method used by Piccolo and Pistone [16, Eq. (9)] and Swift [1, Eq. (61)] for setting volume velocity boundary conditions.

$$M_a = \frac{p_A}{\rho_m a^2} \tag{8}$$

$$M_a = (2 - BR)\frac{|p_A|}{\rho_m a^2}\cos(kx') \tag{9}$$

$$M = \frac{|u_1|}{a} \tag{10}$$

In the 'short stack' approximation familiar to thermoacoustic system designers, M_a may be calculated directly and assumed constant within the stack region. In this study, where the amplitude of the local Mach number varies considerably through the stack region, we will numerically evaluate M at the midspacing and the midlength of the stack region ($x = L_S/2,\ y = 0$) and compare with M_a.

Ishikawa and Mee [13] and Piccolo and Pistone [16] neglected turbulence effects in each of their studies on the basis that the streaming Reynolds number [21], given by

$$N_{R,S} = \frac{|u_1|^2}{\upsilon\omega} \tag{11}$$

was not expected to exceed $(200)^2$ based on the results of Merkli and Thomann [22]. In the context of oscillatory flow, the critical Reynolds number $N^c_{R,S}$ is the condition for which the flow is considered to transition to a turbulent flow regime, that is, the condition for which the Stokes layer becomes unstable [21]. Merkli and Thomann [22] indicated that this transition at $N^c_{R,S}$ is effectively localised to the boundary layer, provided that the boundary layer thickness is significantly less than "other dimensions" such as the tube radius. In other words, the limiting $N^c_{R,S}$ value of $(200)^2$ was developed for internal flows without small features [22]. However, in typical thermoacoustic systems using parallel-plate stacks, the plate thickness is much smaller than the tube radius and could potentially be of similar thickness to the Stokes layer. In this thesis, $N_{R,S}$ values are presented as squared values because they are related to the square of the Reynolds number based upon the boundary layer thickness [22].

The flow impedance created by increasing plate thickness $l = 2t_s$ leads to higher velocities and therefore higher $N_{R,S}$ values within the stack region. Decreasing the blockage ratio (thicker plates) would further increase $N_{R,S}$. Concern that decreasing the blockage ratio would increase $N_{R,S}$ above $(200)^2$ was addressed by considering results from Run 21, which used the lowest (most flow restrictive) blockage ratio (0.7) and highest drive-ratio (8.5%) of the models used in this study.

2.5. Material properties

For the sake of comparison with the results of Ishikawa and Mee [13] and hence the results of other studies using the same operating conditions [10,16], the properties shown in Table 2 are common to all tests in this investigation. Density was approximated using the ideal gas law: constant Prandtl number, specific heats and thermal conductivity were assumed.

Table 2
Flow conditions and material properties used for all computational runs

Property	Value	Units
Operating frequency, f	100	Hz
Ambient temperature, T_m	300	K
Mean pressure, p_m	10	kPa
Gas properties:		
Prandtl number, Pr	0.69	
Thermal conductivity, k_0	0.149	W/m K
Heat capacity, c_p	5200	J/kg K
Dynamic viscosity, μ	2.01×10^{-5}	kg/ms
Ratio of specific heats, γ	1.665	
Plate material properties:		
Thermal conductivity, k_s	10	W/m K
Heat capacity, c_{ps}	400	J/kg K
Density, ρ_s	400	kg/m^3

2.6. Numerical implementation

The commercial CFD software *FLUENT* [23] was used to conduct 2-D simulations of the system. An unsteady formulation was used with first order discretisation of flow. To enable sufficient resolution of each waveform, 100 time steps per period of oscillation (1/100 seconds) were selected, which resulted in a time step size of one ten thousandth of a second (0.1 ms). Convergence criteria for the solution at each time step was based upon the residuals for velocity components and continuity equal to or below 0.01%, and the residual for energy equal to or below 0.0001%.

A mesh spacing of Δx equal to 0.5 mm and Δy equal to 0.16 mm within the stack region (subdomain 'S' shown in Fig. 2) was used, however at increasing axial distances from the stack region, that is, decreasing x for $x \leqslant 0$ and increasing x for $x \geqslant L_S$, Δx was exponentially increased to reflect the increasingly adiabatic (less 'detailed') oscillations present with increasing distance from the stack region. The domains used for Runs 1 to 20 each contained approximately 33,900 nodes. Grid independency was checked using a finer mesh with double the number of mesh intervals n_x, n_y or four times the node density. To match the mesh sizing used in Run 1 of Piccolo and Pistone [16], the x-direction mesh sizing Δx was increased to 1.033 mm whilst Δy was retained at 0.16 mm within the stack region. This resulted in a total of approximately 16,860 nodes used for Run 22.

In the context of numerically modelling thermoacoustic couples, the 'limit state' is not equivalent to an experimental sense, where the limit state is usually observed from stabilisation of measured temperature differences (with orders-of-magnitude larger time constants). Here, the simulation is advanced in time until pressure, velocity and performance measures such as $\Delta T_{k,hx}$ and $\langle \dot{h}_{hx} \rangle_t$ stabilise to within computational error on a cycle to cycle basis. The time-averaged change in enthalpy and entropy flux is identified as reasonably constant in the timeframe for which results are presented.

For each run, a sinusoidal pressure input was applied to the inlet boundary shown in Fig. 3(a) with frequency $f = 100$ Hz and amplitude $|p_1|$ as listed in Table 1. Although an unsteady

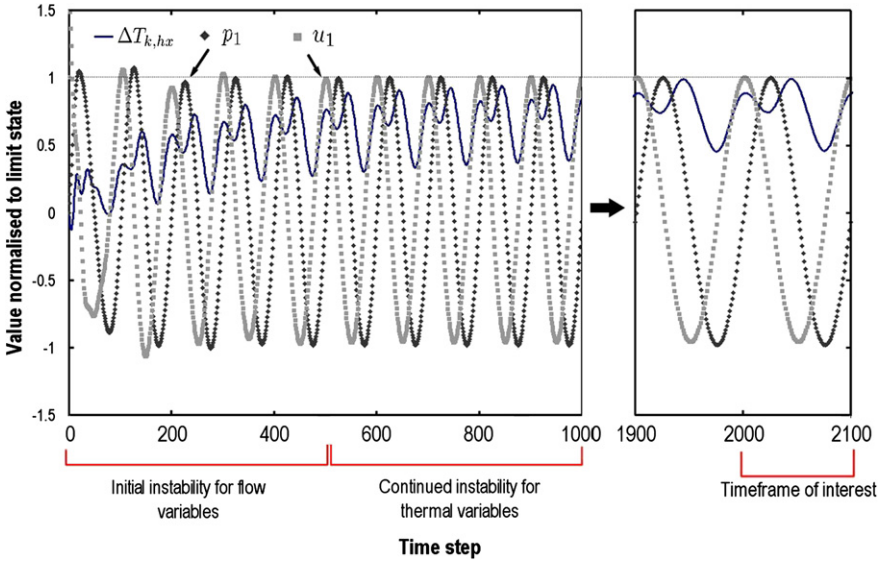

Fig. 4. p_1, u_1 and $\Delta T_{k,hx}$ (Section 2.6.1) at the oscillatory boundary (INLET) versus simulation timesteps 0 to 1000 and 1900 to 2100 for Run 6. Positive velocity is to the right with reference to Fig. 3.

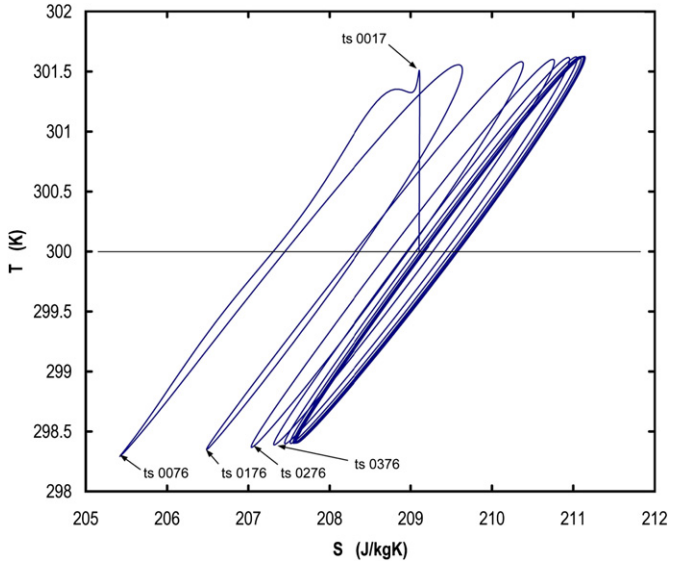

Fig. 5. Temperature versus specific entropy for position 'M1' (0.126 m, 0), over the first ten cycles of Run 1. Points of interest are marked for time steps 0017 (flow-time 0.0017 s), 0076 (flow-time 0.0076 s) and 0176 (flow-time 0.0176 s).

simulation, the model must be initialised such that comparisons between runs can be done under limit or steady state operation. Fig. 4 shows that whilst the pressure and velocity states approach limit state within the first three to four cycles of simulation, Fig. 5 shows that a thermal limit state of the gas within the stack region does not approach limit state until approximately the sixth or seventh cycle. The relative 'distortion' of $\Delta T_{k,hx}$ in Fig. 4 is associated with the incoherent phasing of bulk gas temperature changes at each end of the stack plate.

Two thousand time steps (twenty oscillations) were calculated to initialise each model. An additional 100 time steps (1 full cycle) was then simulated with statistical averaging employed to determine properties such as the time-averaged heat flux distribution or flow parameter.

2.6.1. *Performance scales*

Performance metrics for the model have been developed to identify limit-state operation and for performance comparisons between each mode of operation. The measure of the time-average difference in area-weighted average gas temperature at $x = 0$ and $x = 0.252$ m is defined as

$$\Delta T_{k,hx} = \left\langle \langle T_k \rangle_{x=0.252\ \mathrm{m}} - \langle T_k \rangle_{x=0} \right\rangle_t \tag{12}$$

and could be considered the axial gas temperature difference across the heat exchanging surface, hence the subscript 'hx'.

The distribution of time-averaged heat flux density over an oscillatory cycle at a fluid–solid boundary, $\dot{h}$ is a useful performance measure that has been used in the majority of past studies of thermoacoustic couples. Since previous studies considered a stack plate of zero thickness, this quantity was also referred to as a time-average heat flux in the y-direction, here represented by $\langle \dot{h}_y \rangle_t$. As plates of non-zero thickness will be considered in this study, time-average axial or horizontal heat fluxes through the end tips of the stack plates will exist and shall be denoted by $\langle \dot{h}_x \rangle_t$. The term $\langle \dot{h}_{hx} \rangle_t$ will refer to the time-average heat flux through all fluid–solid boundaries of the stack plate.

The thermodynamic cycles experienced by the gas at fixed positions in the computational domain can also yield insight into the performance of the stack configuration. Table 3 and Fig. 6 indicate fixed positions (using the co-ordinate system shown in Fig. 3(b)) that have been designated as points of interest.

Locations C1, M1 and H1 are located transversely on the line of symmetry at mid-spacing between each plate surface ($y = 0$) and axially within the stack region ($0 \leqslant x \leqslant L_S$). Locations C2, M2 and H2 are transversely located within half the mean thermal penetration distance of the fluid–solid interface, and gas particles here should theoretically experience a greater heat-pumping effect than those on $y = 0$.

A final performance measure used in this study is the energy dissipation rate due to irreversibilities associated with flow dis-

Table 3
Measurement positions of interest

Code	x	y	Comment
C1	0	0	'C' for cold end
M1	$0.5L_S$	0	cf. Position 'M' of Ref. [24]
H1	L_S	0	'H' for hot end
C2	0	$y_{hxsf} - 0.5\delta_{km}$	offset $0.5\delta_{km}$ from plate
M2	$0.5L_S$	$y_{hxsf} - 0.5\delta_{km}$	'M' for midlength
H2	L_S	$y_{hxsf} - 0.5\delta_{km}$	

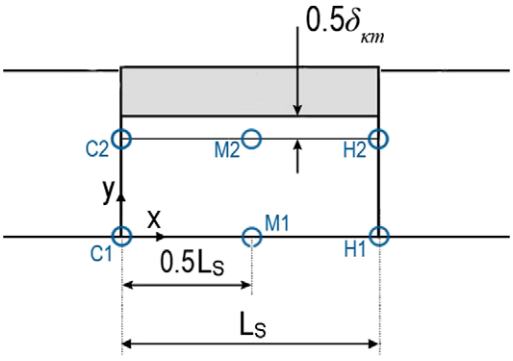

Fig. 6. Diagram indicating measurement points of interest listed in Table 3. Diagram is not to scale.

turbances. With the subdomains A, B, C and S shown in Fig. 2 forming the closed-system volume CV, the entropy rate balance is described by

$$\frac{dS}{dt} = \oint_{CV} \frac{\dot{q}}{T} + \dot{s}_{\text{gen}} \tag{13}$$

and

$$\dot{e}_{\text{diss}} = -T_0 \dot{s}_{\text{gen}} \tag{14}$$

At limit state operation, the time rate of change of entropy of the system dS/dt is considered constant, and since all external boundaries to the model except the 'INLET' boundary are insulated, the rate of energy dissipation due to entropy generation $\dot{e}_{\text{diss}}$ can be approximated using Eq. (14) over a full oscillatory cycle. In this study, the commercial code FLUENT is used to directly measure the volume-average entropy change dS/dt, such that $\bar{\dot{s}}_{\text{gen}}$ is evaluated from

$$\bar{\dot{s}}_{\text{gen}} = \frac{d\bar{S}}{dt} - \int_{\text{INLET}} \frac{\bar{\dot{q}}}{\bar{T}} \tag{15}$$

where the overbar indicates values averaged over a full oscillation. The control volume is expanded to include the plate region and thus account for energy exchanges between the fluid and solid regions.

3. Results

In this section results are presented in terms of the computed flow structures and the rate of heat transportation and dissipation in each run.

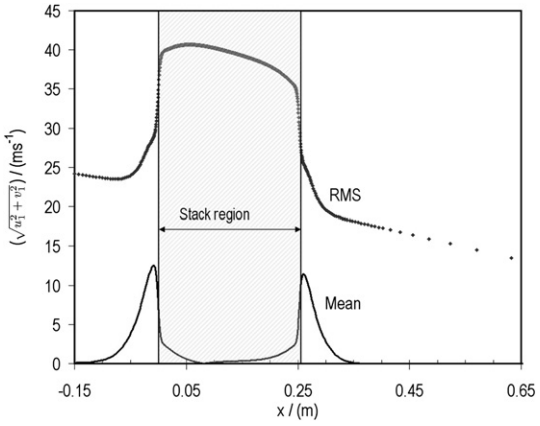

Fig. 7. Estimated distribution of mean and RMS velocity magnitude along the mid-plate spacing ($y = 0$), for the time period 0.2000 s to 0.2100 s. Data shown is for Run 20, with $BR = 0.7$ and $DR = 6.8\%$.

3.1. Flow structures

Discussion of flow structures will be compared with linear estimates of turbulent limits, the generation of flow vortices and velocity gradients.

3.1.1. Comparison with turbulence criteria

It is important to first investigate whether the introduction of the plate thickness $2y_x$ in this study leads to instability of the Stokes boundary layer, since numerical models specific to modelling turbulent behaviour such as the Reynolds Stress Model (RSM) were not incorporated into the computational solver for this study.

Fig. 7 indicates the estimated distribution of mean and RMS velocity magnitude along the mid-plate line ($y = 0$) for Run 20. As expected, the RMS velocity is greater through the stack region due to the reduced cross section with continuous mass flow rate at the stack extremities. However, Fig. 7 shows that whilst the mean velocity is effectively zero at sufficient distance from the stack (which is to be expected at these locations where the flow is theoretically an adiabatic standing wave), there is non-zero mean gas flow at the extremities of the stack. These non-zero mean flows acknowledge that the flow is perturbed by the plate structure and suggest flow recirculation (streaming) effects at these locations.

Table 4 lists the estimated flow parameters used here for the assessment of turbulence. The mean free stream Mach number M as defined in Eq. (10) and the 'acoustic' Mach number M_a as defined in Eq. (8) are also provided in Table 4, where the overbar represents the mean.

The leftmost plate edge at $x = 0$ (which is closer to the velocity antinode in the theoretical half-wavelength resonator) has greater velocities than at $x = L_S/2$ (0.126 m), however the changes in flow disturbance with changes in plate thickness do not allow such straightforward comparison as per Table 4. It can be seen that in the midsection of the stack where x is approximately 0.126 m, the critical Reynolds number criterion for turbulence of $N^c_{R,S} = (200)^2$ as defined by Thompson [21] was not exceeded for Run 21. The conditions used in Run 21 led

Table 4
Predicted $|\bar{u}_1|$, $\bar{M}_a$ and $\bar{M}$ values at Location M1 (Table 3) for each run. $\bar{M}_a|_{L_S/2}$ is found from Eq. (9). $\bar{M}|_{L_S/2}$ is found from Eq. (10). $N_{R,S}|_{L_S/2}$ values reported are maxima

Run	BR	$\lvert\bar{u}_1\rvert_{L_S/2}$ ($\mathrm{m\,s^{-1}}$)	$\bar{M}_a\lvert_{L_S/2}$	$\bar{M}\lvert_{L_S/2}$	$N_{R,S}\lvert_{L_S/2}$
1	1	8.16	0.007	0.0081	$(9.80)^2$
2	1	16.1	0.014	0.0160	$(19.3)^2$
3	1	24.1	0.021	0.0239	$(29.0)^2$
4	1	32.2	0.028	0.0319	$(38.8)^2$
5	0.98	8.38	0.007	0.0083	$(10.0)^2$
6	0.98	16.5	0.014	0.0164	$(19.8)^2$
7	0.98	24.7	0.021	0.0245	$(29.7)^2$
8	0.98	33.1	0.029	0.0328	$(39.7)^2$
9	0.90	9.38	0.008	0.0093	$(11.1)^2$
10	0.90	18.6	0.015	0.0185	$(21.9)^2$
11	0.90	27.8	0.023	0.0276	$(32.8)^2$
12	0.90	37.1	0.031	0.0368	$(43.7)^2$
13	0.80	11.1	0.008	0.0110	$(12.7)^2$
14	0.80	22.0	0.017	0.0218	$(25.4)^2$
15	0.80	32.9	0.025	0.0326	$(37.8)^2$
16	0.80	43.9	0.034	0.0436	$(50.4)^2$
17	0.70	13.5	0.009	0.0134	$(15.3)^2$
18	0.70	26.9	0.018	0.0267	$(30.5)^2$
19	0.70	40.7	0.027	0.0404	$(45.3)^2$
20	0.70	53.4	0.036	0.0530	$(60.3)^2$
21	0.70	66.7	0.046	0.0662	$(75.0)^2$
22	1	8.04	0.007	0.0080	$(9.68)^2$

to the highest reported $|N_{R,S}|$ value of $(75)^2$, or approximately 14% of the $N^c_{R,S}$ limit value.

Table 4 also shows that the numerical result $\bar{M}$ exceeds the calculated $\bar{M}_a$ result by around 10 to 15% for $BR = 1$. As BR increases, the ratio $\bar{M}/\bar{M}_a$ also increases. It is important therefore that whilst the volume velocity through the stack plates is preserved, the transverse distribution in u_1 is perturbed significantly by non-zero y_x, such that excessive errors may arise from use of M_a within stack regions.

3.1.2. Vortex generation

Figs. 8 and 9 illustrate the evolution of flow vortices at the left end of the stack for Run 20, over a full oscillatory period beginning at 0.2028 s, in 1 ms steps. In this timeframe, the flow of gas increases to the left with a velocity maximum at around 0.2052 s which retards to zero at around 0.2077 s. The velocity of the prevailing flow then increases to the right, to again retard to zero at approximately 0.2128 s. Pathlines are generated at selected fluid nodes along $x = 0$ (the left end of the plate) and at distances of 5 and 10 mm in each direction from the y-axis. Pathlines could be considered as massless 'strings' which are useful in visualising the flow structure, and follow streamlines generated at each time step for steady flows. The velocity direction at the inlet is indicated to the left of each figure to show the prevailing velocity in the centre of the device. A scale is provided at the top of each figure to indicate the spatial scales of the vortices generated.

In Fig. 8(a), the fluid is starting to move predominantly left, with fluid closest to the stack plate leading to the left. As the flow shifts to the left, entrained flow over the lip of the plate edge (Fig. 8(b)) results in a small recirculation zone forming (Fig. 8(c)) and growing (Fig. 8(d)) despite the fact that the prevailing flow velocity is now decreasing. This recirculation increases in size until it dominates the flow structure (Fig. 8(e)) and as the flow moves to the right, fluid entrained by the recirculation breaks out to the right and with high velocity streams around the edge of the plate (Fig. 9(a)).

Fig. 9 (a) and (b) shows that the flow of gas entering the domain from upper left becomes increasingly dominant, pushing the recirculation down further. By 0.2098 s (Fig. 9(c)), the recirculation has completely collapsed, and flow upstream of the plate edge begins to approach uniformity. Downstream of the plate, a small recirculation zone is seen to develop (Fig. 9(d)) and the boundary layer thickness increases (Fig. 9(e)). At this timeframe, the prevailing flow is decelerating, and the flow reverses direction as shown by Fig. 8(a) to again repeat the cycle.

It can be seen that the structure shown in Fig. 8(c) is similar to the result presented by Blanc-Benon et al. [18]. Although Run 20 uses helium for a working gas compared with air in the Blanc-Benon et al. result, and the two figures are produced for different time values two hundredths of a phase apart, the shapes of each vortex generated are proportionately similar. The formation of separation zones on the plate inside edge in Fig. 9 (c) to (e) was also demonstrated by Worlikar and Knio [11] for much lower drive-ratios ($DR \leqslant 1\%$).

3.1.3. Entropy generation

Fig. 10 presents the rate of entropy generation $\dot{s}_{\mathrm{gen}}$ with respect to drive-ratio DR for Runs 1 to 21, grouped by blockage ratio. This figure shows the increase in entropic losses with increasing plate thickness $2y_x$ and drive-ratio DR, against previous results from Ishikawa and Mee [13] and the analytical result obtained using an expression from Swift [1, Eq. (89)] with BR set to 0.7. The increase in rate of entropy generation $\dot{s}_{\mathrm{gen}}$ with drive-ratio is shown to be quadratic, a finding made by Ishikawa and Mee for a plate of zero thickness [13].

It can be seen that the entropy generation rate $\dot{s}_{\mathrm{gen}}$ obtained using a thermoacoustic couple modelled with zero thickness in the present study is approximately 40% higher than that calculated by Ishikawa and Mee. However this result is attributed in part to use of a mesh density five times greater in the axial direction than that used previously by Ishikawa and Mee. Whilst the axial dimension of subdomain 'A' (Fig. 2) is also noted to be approximately 75% greater than the equivalent region in the domain used by Ishikawa and Mee [13], the zones in which the rate of entropy generation is significant are well within regions common to both models.

The analytical result of $\dot{s}_{\mathrm{gen}}$ for $BR = 0.7$ utilising Eq. (89) of Swift [1] is shown to exceed the numerical results of Ishikawa and Mee by typically 13 to 15%. This is expected since the viscous shear dissipation component was calculated with the gas velocity u_1 increased using the blockage ratio as shown in Eq. (9) which in turn increases $\dot{s}_{\mathrm{gen}}$.

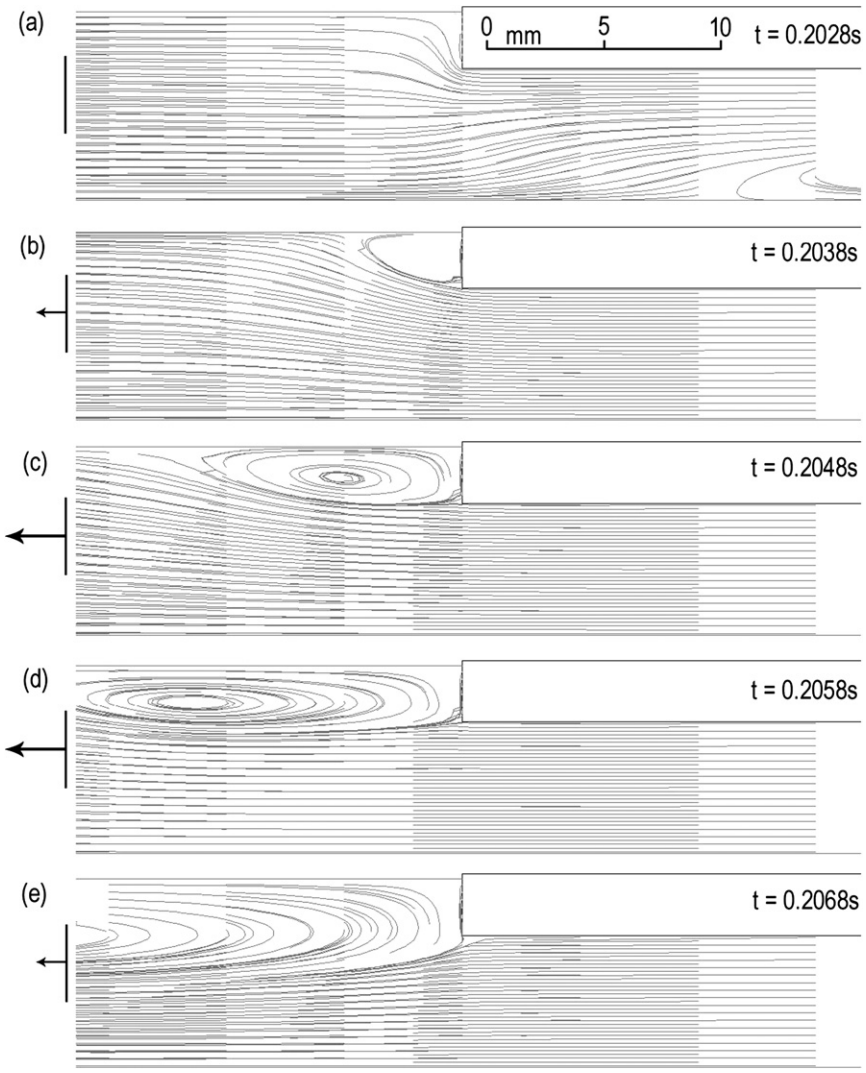

Fig. 8. Flow pathlines for Run 20, at (a) $t = 0.2028$ s, (b) $t = 0.2038$ s, (c) $t = 0.2048$ s, (d) $t = 0.2058$ s, (e) $t = 0.2068$ s. The prevailing flow direction and velocity magnitude are indicated to the left of each figure.

3.2. Heat transportation

3.2.1. Comparison with other models

Fig. 11 indicates the time-averaged heat flux across the plate surface in the y-direction $\dot{h}_y$ versus axial position x for Run 22 of the current study and Run 1 of Piccolo and Pistone [16]. In forming good agreement with Run 1 of Piccolo and Pistone [16], and hence Run 7 of Ishikawa and Mee [13] and Run 2 of Cao et al. [10], the numerical method used is considered appropriate for the simulation of thermoacoustic couples with zero thickness. Slight differences are expected as the temperature at the surface of the plate is not fixed at T_0 in the present study.

In regards to heat transfer, the sign conventions used in this paper are such that the plate is a control volume, so a negative $\dot{h}_y$ value indicates net heat transfer from the plate to the working fluid and a positive $\dot{h}_y$ value indicates net heat transfer from the working fluid to the plate [25]. The time-average heat flux across the plate surface in a thermoacoustic couple is shown to be concentrated to the extremities or edges of the plate surface, and appears symmetric across the plate midpoint. In fact, the distribution of $\dot{h}_y$ is asymmetric in a thermoacoustic couple, for reasons such as the variance in velocity amplitude between each end of the stack. Fig. 11 appears symmetric since the thickness of the plate is not modelled. Run 1 indicates that the point at which $\langle \dot{h}_y \rangle_t = 0$ is not $x = 0.5L_S$, but rather $x \approx 0.2L_S$. We attribute this to a broad shift in $\dot{h}_y$ across the plate surface.

3.2.2. Thermophysical cycles

In Fig. 12, temperature–entropy curves are plotted for selected locations of Run 1 at limit state. It can be seen that the oscillations of the gas at location M1 are effectively adiabatic, however the cycles experienced at locations C1 and H1 are noticeably different. Locations C1 and H1 are located along $y = 0$, at more than three times the mean thermal penetration distance from the plate surface. However, the T–s curve at these two locations are perturbed: the T–s curve is expanded at locations C1 and H1 for approximately 270° of the limit cycle. The perturbances of C1 and H1 also occur at opposite phases in the cycle, for predominantly negative p_1 at location C1 and predominantly positive p_1 at location H1. This suggests that ef-

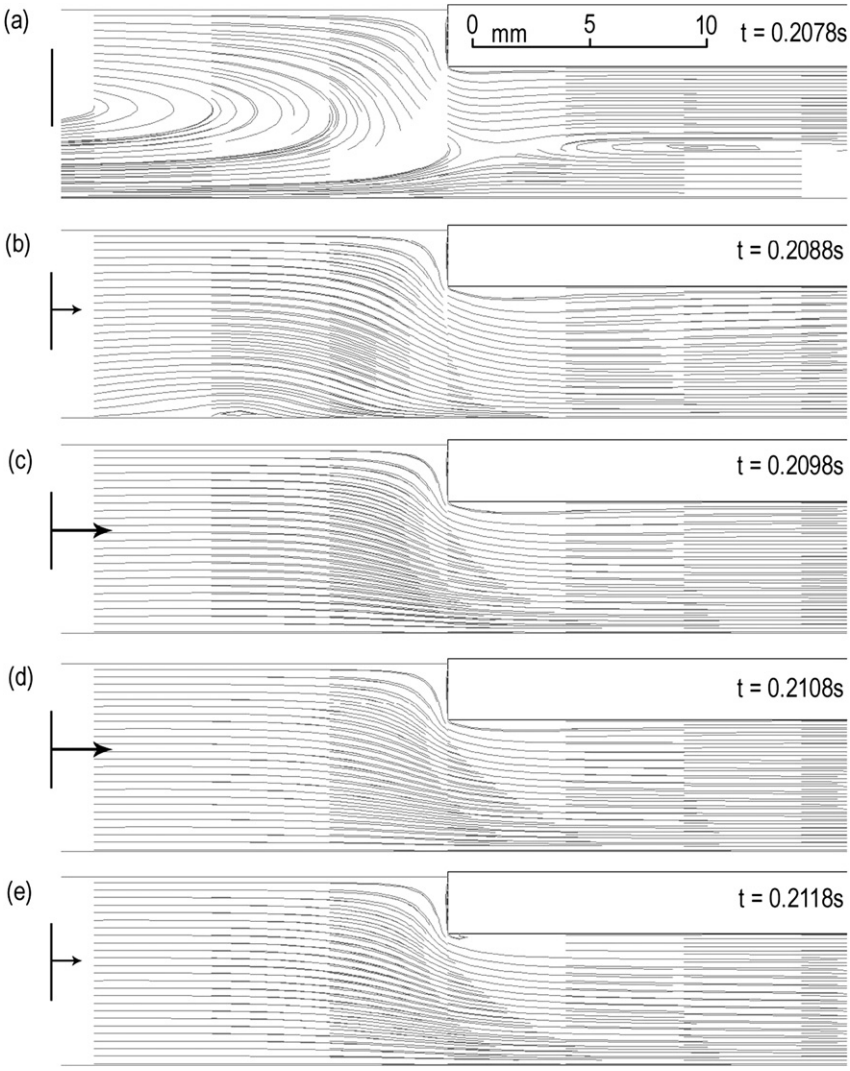

Fig. 9. Flow pathlines for Run 20, at (a) $t = 0.2078$ s, (b) $t = 0.2088$ s, (c) $t = 0.2098$ s, (d) $t = 0.2108$ s, (e) $t = 0.2118$ s. The prevailing flow direction and velocity magnitude are indicated to the left of each figure.

fective heat transportation is occurring at these locations despite their distance to the stack plate being significantly greater than the thermal penetration depth. It is feasible that flow recirculations at the plate extremities (Figs. 7, 9(a)) may lead to fluid at distances greater than $\delta_{\kappa m}$ participating in heat transfers with the plate.

Figs. 13 and 14 plot temperature versus specific entropy for selected locations of both Run 4 and Run 20 during limit state operation. The major difference between Runs 4 and 20 is the value of y_x: Run 4 considers the plate to be of zero thickness, whereas Run 20 models the plate as 2.4 mm thick. The perturbation to the temperature-specific entropy curve is significant, not only at locations at the edges of the plate but also at the mid-plate locations 'M1' and 'M2'.

In Fig. 13, indicators 'A' and 'B' designate features of the curve specific to flow disturbances over each plate edge. The value indicated by 'A' is obtained at a flow time of 0.2082 s, between the timeframes used in Fig. 9 (a) and (b). As can be seen from these two frames, the specific entropy at Location C1 during that short time period is boosted from excess energy

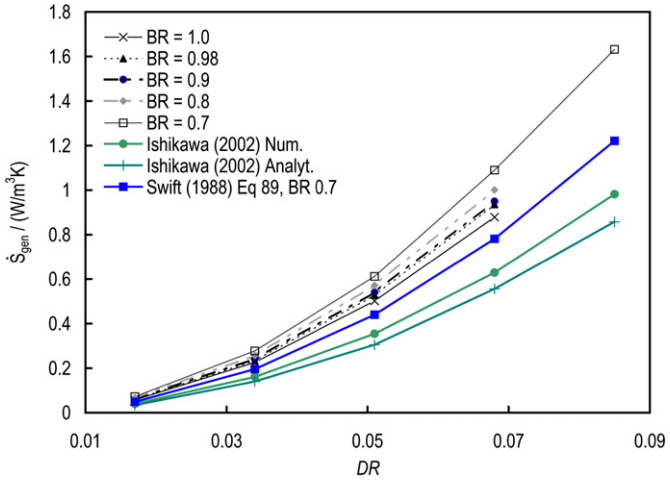

Fig. 10. Rate of entropy generation $\dot{s}_{\text{gen}}$ versus drive-ratio DR, with selected runs grouped by blockage ratio, as follows: $BR = 1.0$ (Runs 1 to 4), $BR = 0.98$ (Runs 5 to 8), $BR = 0.9$ (Runs 9 to 12), $BR = 0.8$ (Runs 13 to 16), $BR = 0.7$ (Runs 17 to 21). The analytical result of Swift was generated using Eq. (89) of Ref. [1].

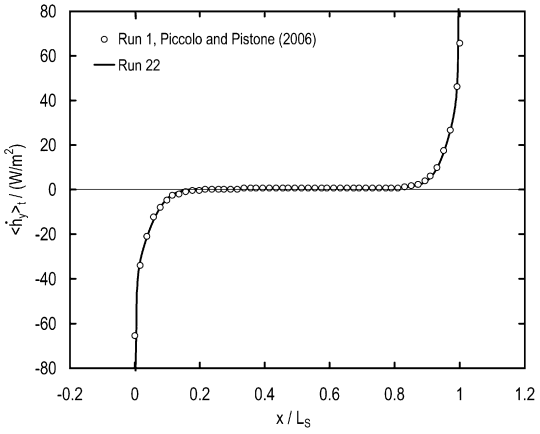

Fig. 11. Distribution of time-averaged heat flux in the y-direction $\langle \dot{h}_y \rangle_t$ along the horizontal plate surface according to axial position x. Open circles are approximate numerical data from Run 1 of Ref. [16]. Positive $\dot{h}_y$ indicates net heat transfer from the working fluid to the plate.

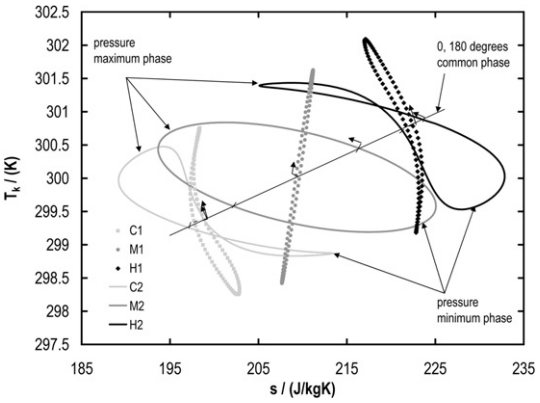

Fig. 12. Temperature versus entropy cycles for selected fixed positions defined in Table 3 at limit state for Run 1. The position and direction of the cycle at ts 2000 (flow time 0.2 s) is indicated with a solid arrow. Phases of maximum and minimum pressure are indicated for Locations C2, M2 and H2.

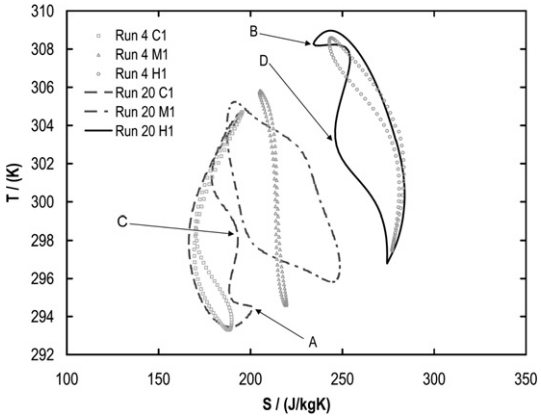

Fig. 13. Limit state behaviour of temperature versus specific entropy at Locations C1, M1 and H1 for Runs 4 and 20.

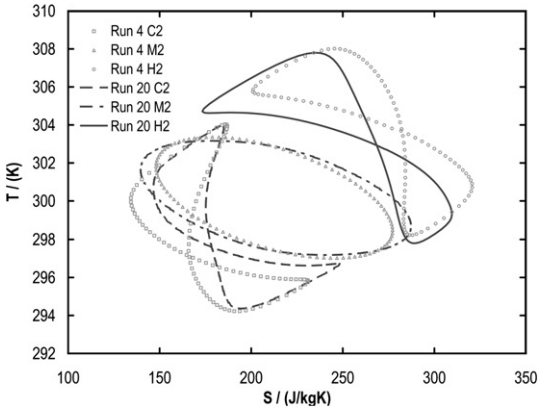

Fig. 14. Limit state behaviour of temperature versus specific entropy at Locations C2, M2 and H2 for Runs 4 and 20.

dissipation from the collapsing vortex upstream of the flow. The same effect, occurring with opposite phase at the other end of the plate, is indicated by 'B' in Fig. 13.

Indicators 'C' and 'D' in Fig. 13 point to phases in the cycle for which the flow velocity into the stack region (rightward for Location 'C1', leftward for Location 'H1') is greatest. This phase in the cycle for Location 'C1' occurs between the timeframes used in Fig. 9 (c) and (d).

A heat pumping effect can be seen from comparison of Figs. 13 and 14 in the temperature bias to the 'H1' and 'H2' ends. The distorted 'folded' or 'figure of 8' curves at Locations 'C2' and 'H2' indicate that there is an effective transfer of heat, whereas the open, elliptical shape of the curve for Location 'M2' indicates a storage of potential energy instead. This result is expected since whilst Locations 'C2' 'M2' and 'H2' are all located $\delta_\kappa/2$ transversely from the plate, Fig. 11 shows that the time-average heat transfer to the plate occurs only at the plate edges (Location 'M2' is at the midpoint).

The effect of plate thickness is also seen to reduce the performance of the plates, in that the average temperatures in Run 20 (compared to Run 4) are lower at the 'hot' end (Locations 'H1' and 'H2') and higher at the 'cold' end (Locations 'C1' and 'C2').

3.2.3. Evolution of thermoacoustic couple heat flux distribution

The evolution of the distribution of transverse heat flux $\dot{h}_y$ through the plate surface for Run 1 is shown in Fig. 15. The surface plot is given for the 0.2 to 0.21 s timeframe of interest, and negative heat flux as shown indicates heat transfer from fluid to the plate (i.e. cooling of the surrounding gas). Fig. 16 shows the same result for Run 20, which differs to Run 1 in blockage ratio (0.7 in Run 20 to 1) and drive ratio (6.8% in Run 20 to 1.7%). It is important to note that whilst Figs. 15 and 16 do not include axial heat flux $\dot{h}_x$ via the edges of the stack plate, this component of the overall heat flux through the solid-fluid boundary $\dot{h}_{hx}$ is significant (Section 3.2.4).

The results shown in Figs. 15 and 16 demonstrate the phasing of heat transfer in such detail that the cycle can be broken down into four distinct phases of compression, heating, expansion and cooling, each of 90° phase duration, in similar fashion to most studies discussing the operation of standing wave thermoacoustic devices [1,26]. At 0.2 s, the positive (rightward) velocity maximum should denote the midpoint of the compression phase, since at this point in time, the pressure is increasing and

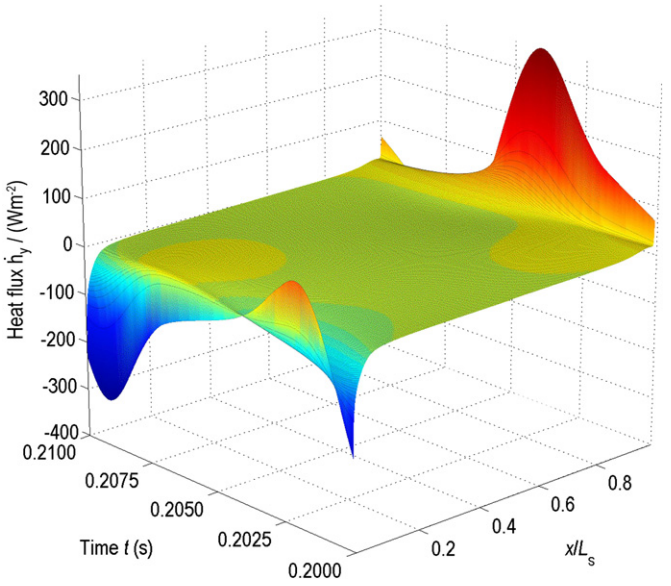

Fig. 15. Surface plot of transverse heat flux $\dot{h}_y$ through the horizontal plate surface for the limit state cycle of Run 1.

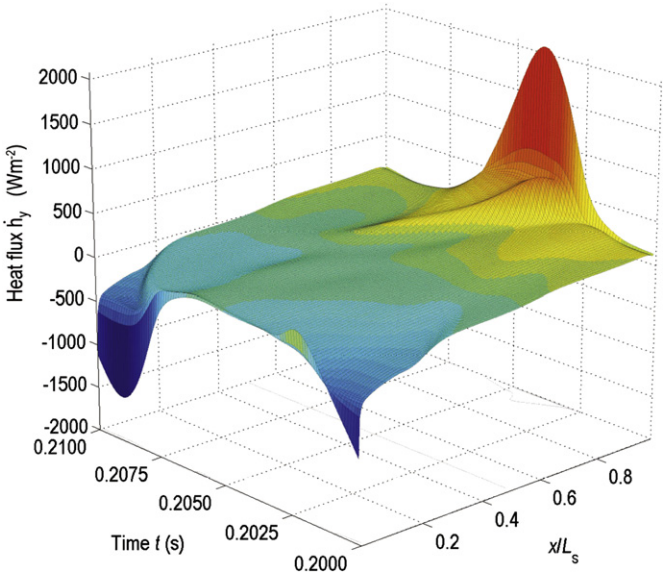

Fig. 16. Surface plot of transverse heat flux $\dot{h}_y$ through the horizontal plate surface for the limit state cycle of Run 20. Note the difference z-axis scaling to Fig. 15.

the velocity is decreasing from a maximum (Fig. 9 (c) and (d)). However, thermal delays in the system are present and so there exists a phase delay in the commencement of each cycle.

At around 0.2012 s for Run 1, the heating phase is apparent, with heat transfer to the fluid occurring at both ends of the thermoacoustic couple at this instant. The cycle then shifts to an expansion phase which begins at around 0.2037 s, and leads to the cooling phase denoted by the significant decrease in $\dot{h}_y$ near $x/L_S = 0$. The flow structure about $x/L_S = 0$ during the cooling phase for Run 20 is captured in Fig. 9 (a) to (c).

In both Figs. 14 and 15, $\dot{h}_y$ is shown to be oscillatory at both ends, with a superimposed heat flux proportional to the oscillatory pressure. At around $t = 0.2037$ s near $x/L_S = 1$,

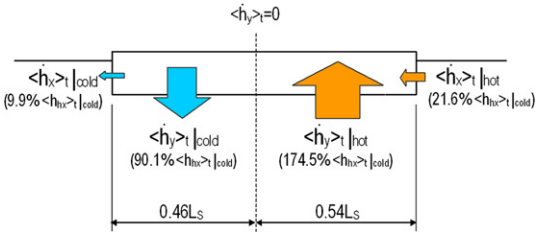

Fig. 17. Sketch showing the proportion of time-averaged heat flux through the plate surface for limit-state operation of Run 20. Percentage values quoted are referenced to the total heat flux entering the plate over an oscillatory cycle, $\langle\dot{h}_{hx}\rangle_t|_{cold}$.

an additional increase in $\dot{h}_y$ is noted, with a decrease around $t = 0.2087$ s near $x/L_S = 0$ also noticeable. These two variations or 'spikes' from the prevailing $\dot{h}_y$ distribution in Run 1 are captured by the time-averaged measure $\langle\dot{h}_y\rangle_t$ such as that presented in Fig. 11. These spikes are more apparent in Run 20 (Fig. 16).

3.2.4. Plate edge heat transfer

The results so far presented have demonstrated a thermoacoustic heat-pumping effect from the left side ($x = 0$) to the right side ($x = 0.252$ m) of the plate. Time-averaged temperatures of gas in the vicinity of the left side have decreased, and temperatures on the right side have increased.

Fig. 17 shows the relative magnitude of axial heat flux through the plate ends in comparison to transverse heat flux through the plate facing for Run 20. The time-averaged heat flux via each of the left ('cold') and right ('hot') plate ends $\langle\dot{h}_x\rangle_t|_{cold}$ can be compared to the time-averaged heat fluxes $\langle\dot{h}_y\rangle_t|_{cold}$ and $\langle\dot{h}_x\rangle_t|_{hot}$ through the plate horizontal surface. For Run 20, the point at which the time-average transverse heat flux is zero was found to be slightly closer to the cold end of the plate (4% of L_S). The transverse heat flux through surfaces forming the physical ends of the plate is shown by Fig. 17 to be significant fractions of the total heat flux through the plate.

3.2.5. Effect of blockage ratio upon heat transfer rate

Fig. 18 shows that increases in y_x and hence decreases in blockage ratio BR lead to a larger integral of $\langle\dot{h}_{hx}\rangle_t$ and hence the performance of the thermoacoustic couple. This performance increase comes at the expense of increased entropy losses, as discussed in Section 3.1.3.

Fig. 19 presents the performance criterion $\Delta T_{k,hx}$ normalised by the result obtained using Runs 1 to 4 with a blockage ratio of 1, versus the drive-ratio. This figure compares the increase in temperature difference across the stack with increasing y_x and DR. For a drive-ratio of 1.7%, it can be seen that the performance of the stack is reduced with increasing plate thickness $2y_x$. However, for all drive-ratios above 3% considered, the performance of the thermoacoustic couple was actually better than the zero-thickness condition ($BR = 1$). Regardless of drive-ratio, it is evident that for thermoacoustic couples of rectangular cross section, maximising BR will enable an increase in the performance scale $\Delta T_{k,hx}$. However the influence of subdomain 'H' (Fig. 2) may be significant at such a small plate thickness and actually a source of error here. As we seek to

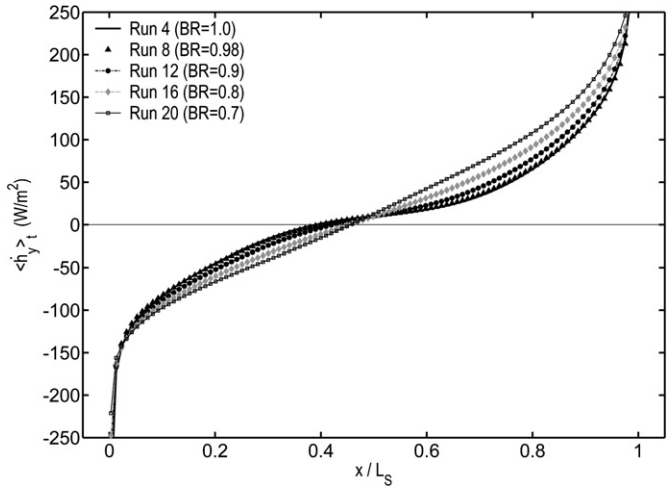

Fig. 18. Comparison of time average transverse heat flux for $DR = 6.8\%$ and increasing BR. Data shown is for Run 4 ($y_x = 0$), Run 8 ($y_x = 0.16$ mm), Run 12 ($y_x = 0.8$ mm), Run 16 ($y_x = 1.6$ mm), and Run 20 ($y_x = 2.4$ mm).

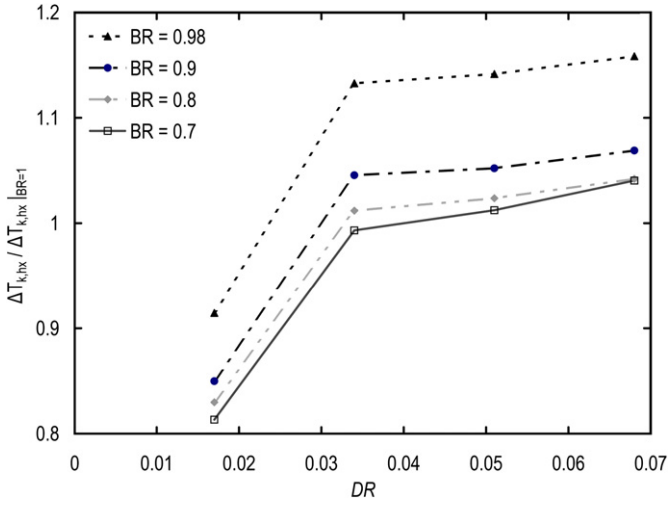

Fig. 19. $\Delta T_{k,hx}$ normalised by same result obtained using a blockage ratio BR of 1 (Runs 1 to 4) versus drive-ratio DR. Data is presented from Runs 5 to 8 ($BR = 0.98$), Runs 9 to 12 ($BR = 0.9$), Runs 13 to 16 ($BR = 0.8$) and Runs 17 to 20 ($BR = 0.7$).

move away from models of zero thickness plates, it is perhaps beyond the scope of the paper to quantify its influence.

As noted by Poese [27], drive-ratios above 3% cannot be expected to correspond to a linear increase in the performance of the stack, and this is shown by Fig. 19: the normalised $\Delta T_{k,hx}$ does not increase linearly with DR at drive-ratios above 3%, and higher order effects such as the increased rate of entropy generation and viscous losses are considered contributors to this result. Interestingly, the performance increase from $DR = 5.1\%$ to $DR = 6.8\%$ is noticeably greater than $DR = 3.4\%$ to $DR = 5.1\%$, although a specific cause for this result is as yet unidentified.

4. Conclusions

Results indicate that the parameter y_x strongly controls the generation of vortices outside the stack region and perturbs the flow structure and heat flux distribution at the extremities of the plate. An increase in y_x is also shown to improve the integral of the total heat transfer rate and gas temperature difference across the stack ($\Delta T_{k,hx}$) but at the expense of increased entropy generation.

In practice, typical parallel or rectangular section stacks do not have perfectly square edges. With existing literature considering only rectangular or zero-thickness (1-D) plates, it would be interesting to see if gains in performance could be achieved using non-rectangular cross sections, such as rounded or elliptical shaped edges. The model system shown here is currently being modified to provide for the investigation of non-rectangular shapes such as rounded or aerofoil cross sections.

References

[1] G. Swift, Thermoacoustic engines, J. Acoust. Soc. Am. 84 (4) (1988) 1145–1180.
[2] G. Swift, Thermoacoustics: A Unifying Perspective for Some Engines and Refrigerators, Acoustical Society of America, 2002.
[3] N. Rott, Thermoacoustics, Adv. Appl. Math. 20 (1980) 135–175.
[4] B. Ward, J. Clark, G. Swift, Design Environment for Low-Amplitude ThermoAcoustic Energy Conversion (DeltaEC) User's Guide (Version 6.0), Los Alamos National Laboratory, October 2007.
[5] M. Wetzel, C. Herman, Design optimisation of thermoacoustic refrigerators, Int. J. Refrig. 20 (1) (1997) 3–21.
[6] S. Backhaus, G. Swift, A thermoacoustic-Stirling heat engine: Detailed study, J. Acoust. Soc. Am. 107 (2000) 3148–3166.
[7] S. Backhaus, G. Swift, Fabrication and use of parallel plate regenerators in thermoacoustic engines, Proceedings from the 36th Intersociety Energy Conversion Engineering Conference (IECEC) 1 (2001) 1393–1398.
[8] S. Backhaus, E. Tward, M. Petach, Traveling-wave thermoacoustic electric generator, Appl. Phys. Lett. 85 (6) (2004) 1085–1087.
[9] D. Gardner, G. Swift, A cascade thermoacoustic engine, J. Acoust. Soc. Am. 114 (4) (2003) 1905–1919.
[10] N. Cao, J. Olsen, G. Swift, S. Chen, Energy flux density in a thermoacoustic couple, J. Acoust. Soc. Am. 99 (6) (1996) 3456–3464.
[11] A. Worlikar, O. Knio, Numerical simulation of a thermoacoustic refrigerator. I. Unsteady adiabatic flow around the stack, J. Comp. Phys. 127 (2) (1996) 424–451.
[12] E. Besnoin, Numerical study of thermoacoustic heat exchangers, PhD thesis, The Johns Hopkins University, Baltimore, Maryland, 2001.
[13] H. Ishikawa, D. Mee, Numerical investigations of flow and energy fields near a thermoacoustic couple, J. Acoust. Soc. Am. 111 (2) (2002) 831–839.
[14] D. Marx, P. Blanc-benon, Computation of nonlinear and EDGE effects in a thermoacoustic refrigerator, in: Proceedings of the 7th Biennial Conference on Engineering Systems Design and Analysis, 2004, pp. 253–262.
[15] E. Besnoin, O.M. Knio, Numerical study of thermoacoustic heat exchangers, Acta Acustica United with Acustica 90 (2004) 432–444.
[16] A. Piccolo, G. Pistone, Estimation of heat transfer coefficients in oscillating flows: The thermoacoustic case, Int. J. Heat Mass Transfer 49 (2006) 1631–1642.
[17] J. Wheatley, T. Hofler, G. Swift, A. Migliori, An intrinsically irreversible thermoacoustic heat engine, J. Acoust. Soc. Am. 74 (1) (1983) 153–170.
[18] P. Blanc-Benon, E. Besnoin, O. Knio, Experimental and computational visualization of the flow field in a thermoacoustic stack, C. R. Mecanique 331 (2003) 17–24.
[19] S. Duffourd, Refrigerateur thermoacoustique: etudes analytiques et experimentales en vue d'une miniaturisation, PhD thesis, Ecole Centrale de Lyon, 2001.
[20] H. El-Gendy, Y.S. Kwon, L. Lyard, O.G. Symko, Optimization of miniature thermoacoustic coolers, Acoustics Today 2 (3) (2006) 44–45.
[21] C. Thompson, Stability of a stokes boundary layer, J. Acoust. Soc. Am. 81 (4) (1987) 861–873.

[22] P. Merkli, H. Thomann, Transition to turbulence in oscillating pipe flow, J. Fluid Mech. 68 (3) (1975) 567–575.
[23] FLUENT 6.2.16 User Manual, Technical report, Fluent Inc., 2006.
[24] D. Marx, P. Blanc-Benon, Computation of the temperature distortion in the stack of a standing wave thermoacoustic refrigerator, J. Acoust. Soc. Am. 118 (5) (2005) 2993–2999.
[25] A.F. Mills, Heat Transfer, second ed., Prentice Hall, Englewood Clifs, NJ, USA, 1999.
[26] P. Ceperley, A pistonless Stirling engine—the traveling wave heat engine, J. Acoust. Soc. Am. 66 (5) (1979) 1508–1513.
[27] M. Poese, S. Garrett, Performance measurements on a thermoacoustic refrigerator driven at high amplitudes, J. Acoust. Soc. Am. 107 (2000) 2480–2486.